ACS Energy LETTERS

http://pubs.acs.org/journal/aelccp

Discovery of Manganese-Based Solar Fuel Photoanodes via Integration of Electronic Structure Calculations, Pourbaix Stability Modeling, and High-Throughput Experiments

Aniketa Shinde,[†,◆] Santosh K. Suram,[†,◆] Qimin Yan,[‡,§,∥,◆] Lan Zhou,[†] Arunima K. Singh,[#] Jie Yu,[†,∥,⊥,#] Kristin A. Persson,[*,⊥,∇] Jeffrey B. Neaton,[*,‡,§,#,¶] and John M. Gregoire[*,†]

[†]Joint Center for Artificial Photosynthesis, California Institute of Technology, Pasadena, California 91125, United States
[‡]Molecular Foundry, Lawrence Berkeley National Laboratory, Berkeley, California 94720, United States
[§]Department of Physics, University of California, Berkeley, California 94720, United States
[∥]Department of Physics, Temple University, Philadelphia, Pennsylvania 19122, United States
[⊥]Environmental Energy Technologies Division, Lawrence Berkeley National Laboratory, Berkeley, California 94720, United States
[#]Joint Center for Artificial Photosynthesis, Lawrence Berkeley National Laboratory, Berkeley, California 94720, United States
[∇]Department of Materials Science and Engineering, University of California, Berkeley, California 94720, United States
[¶]Kavli Energy NanoSciences Institute at Berkeley, Berkeley, California 94720, United States

Ⓢ *Supporting Information*

ABSTRACT: **The solar photoelectrochemical generation of hydrogen and carbon-containing fuels comprises a critical energy technology for establishing sustainable energy resources. The photoanode, which is responsible for solar-driven oxygen evolution, has persistently limited technology advancement due to the lack of materials that exhibit both the requisite electronic properties and operational stability. Efforts to extend the lifetime of solar fuel devices increasingly focus on mitigating corrosion in the highly oxidizing oxygen evolution environment, motivating our development of a photoanode discovery pipeline that combines electronic structure calculations, Pourbaix stability screening, and high-throughput experiments. By applying the pipeline to ternary metal oxides containing manganese, we identify a promising class of corrosion-resistant materials and discover five oxygen evolution photoanodes, including the first demonstration of photoelectrocatalysis with Mn-based ternary oxides and the introduction of alkaline earth manganates as promising photoanodes for establishing a durable solar fuels technology.**

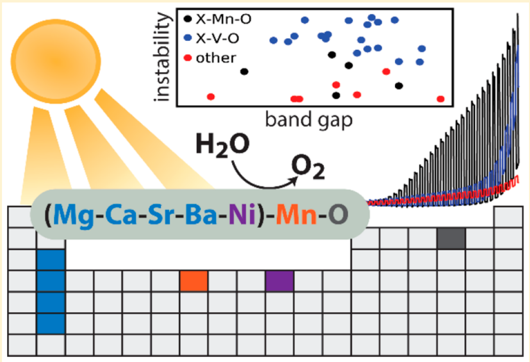

Solar photo(electro)catalysts comprise a class of materials that enable harvesting of solar energy to perform chemistries of critical importance for society, from water purification to fuel synthesis.[1] Despite the critical function of Mn-oxo clusters in the quintessential solar harvester, Photosystem II,[2] implementations of Mn-based materials in solar and energy technologies have largely been limited to dark catalysts,[3] creating a long-standing question as to whether Mn-based oxides can be made photoactive. By combining the broad range of Mn−O chemistries with an additional cation, a variety of crystal structures and electronic structures may be accessed. To explore the existence of photoanodes in this vast ternary oxide material space, we developed and deployed an accelerated discovery pipeline that integrates theory and experiment to both identify promising materials and establish relationships among their functional properties and underlying physical chemistry.

Semiconductor materials used as photocatalysts, particularly in aqueous photoelectrochemistry, are often not thermodynamically stable under operating conditions, typically yielding one of two scenarios: (i) self-passivation wherein preferential corrosion of one or more elements alters the surface

Received: July 10, 2017
Accepted: September 7, 2017
Published: September 7, 2017

ACS Publications

DOI: 10.1021/acsenergylett.7b00607
ACS Energy Lett. 2017, 2, 2307−2312

composition until a stable layer is formed[4] or (ii) gradual to rapid corrosion of the entire semiconductor.[5] For solar fuel photoanodes that drive the oxygen evolution reaction (OER), recent efforts have focused on the development of protective layers to mitigate electrolyte contact to the semiconductor, which is an effective approach for self-passivating materials and impractical otherwise because a single-point defect in the protective coating inevitably results in complete corrosion of the semiconductor.[6] Optimal photoanode coatings must mitigate surface recombination and enhance hole extraction from the semiconductor; to develop such coatings, it is desirable to alleviate the corrosion-protection mandate, motivating the search for new operationally stable photoanode materials.[7−9] Thermodynamic stability under the highly oxidizing OER environment is a tall order with Fe_2O_3,[10] $ZnFe_2O_4$,[11,12] and Bi_2MoO_6[13] being the only visible band gap metal oxide photoanodes that exhibit such stability (see below), prompting our concerted effort to identify photoanode materials that mitigate the thermodynamic instability under operating conditions.

We recently established a seven-tier screening pipeline integrating theory and experiment and applied it to identification of OER photoanodes among ternary metal vanadates with a VO_4 structural motif.[14] The pH 9.2, borate-buffered electrolyte in that work was chosen due to the operational stability exhibited by several of the early photoanode discoveries in this electrolyte.[15,16] While this empirical establishment of suitable photoelectrochemical screening conditions enabled rapid identification of 12 new photoanode phases, a robust mechanism to identify suitable conditions has not been established, which we address in the present work with computationally guided experiment design. This deeper integration of theory and experiment employs an extension of the Materials Project[17] Pourbaix Application (Pourbaix App) by identifying a materials-specific electrolyte pH range in which the material is most thermodynamically stable under operating conditions.

For ternary Mn-based oxides, the stability of MnO_2 above 1.23 V vs RHE over a substantial pH range[17] not only promotes stabilization of the ternary oxide but may also provide a self-passivation layer if necessary, making this class of materials particularly promising for photoanode discovery. To initiate the screening pipeline (Figure 1), the Materials Project database was mined for X−Mn−O phases, where X is one of the following 25 elements: Ba, Bi, Ca, Ce, Co, Cu, Cr, Fe, Ge, La, Mg, Mo, Nb, Ni, Sb, Sc, Si, Sn, Sr, Ti, V, W, Y, Zn, or Zr. The set of elements was chosen under consideration of factors such as earth-abundance, span of oxidation states, presence in known OER photoanodes, representation of various classes of cations including alkaline earth, transition metal, lanthanide, and rare earth elements, and convenience of deposition in reactive cosputtering with Mn. The resulting 338 X−Mn−O phases available in the Materials Project comprise tier 1 of the screening pipeline.

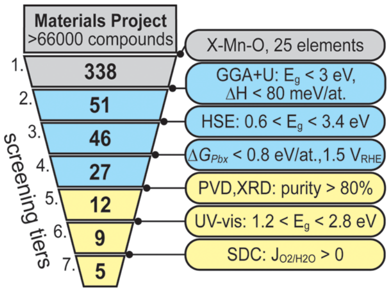

Figure 1. Tiered screening pipeline for accelerated discovery of solar fuel photoanodes. The number of compounds (bold) and screening criteria used in this study for the seven-tier pipeline that integrates database mining (gray), high-throughput computational screening (blue), and high-throughput experimental screening (yellow).

Tier 2 down selection proceeded using existing Materials Project band gaps and enthalpies of formation computed from density functional theory (DFT) within the generalized gradient approximation (GGA) and Hubbard U corrections (GGA+U).[18] The upper threshold values of 3 eV and 80 meV $atom^{-1}$, respectively, were chosen with consideration of the known systematic errors in these computed band gap values and the absence of kinetic and entropic considerations in the database enthalpy values. Band gap calculations for selecting tier 3 phases incorporated the HSE hybrid functional with a default exact-exchange mixing parameter value of 25%. The target band gap range of 1.2−2.8 eV was expanded by ±0.6 eV to account for the approximate nature of these band gap calculations.[19,20]

The detailed evaluation of the X−Mn−O phases proceeded with a final computational screen based on the energetic (in)stability of the phases in aqueous environments under operating conditions. At a given pH and electrochemical potential, the metal oxide phase is either thermodynamically stable, in which case it lies on the energy hull of the Pourbaix diagram, or it lies at a Gibbs free energy ΔG_{pbx} above the Pourbaix hull. To evaluate the Pourbaix stability of each phase, an electrochemical potential of 1.5 V vs RHE was chosen as it corresponds to an OER overpotential of approximately 0.27 V, at which the best OER electrocatalysts yield reaction rates relevant for solar fuels generation.[21] That is, presently known kinetic limitations of the OER require the potential of photogenerated holes to be in excess of 1.5 V vs RHE, and for stable photoelectrochemical operation, it is desirable for the photoanode material to not corrode at the equivalent electrochemical potential. To identify photoanodes for essentially any solar fuel generator involving water, including water splitting and CO_2 reduction technologies, we screened for stability over a broad pH 0−14 window by calculating ΔG_{pbx} at all 15 pH units in this range and requiring that the minimum above-hull energy be below 0.8 eV $atom^{-1}$. Even with this fairly large above-hull threshold, less than 60% of the phases passed to tier 4 of the pipeline.

The computational screening portion of the pipeline yielded 27 phases targeted for experimental screening. Multiple thin-film libraries containing each target cation composition were synthesized with different processing conditions, yielding in total 12 target phases with sufficient phase purity (see Supporting Information Table S1). Optical spectroscopy experiments indicated that the band gap of three of these is above 2.8 eV, outside of the target range. Photoelectrochemistry (PEC) experiments on the remaining nine phases (tier 6) were guided by Pourbaix calculations by selecting two or three of the following electrolytes in which the phase exhibits the best Pourbaix stability: pH 2.9 (phosphate-acid buffer), pH 6.8 (phosphate-base buffer), pH 10 (borate buffer), or pH 13 (sodium hydroxide). The electrolyte selections and resulting identification of photoactivity are summarized in Figure 2a, which also shows the ΔG_{pbx} data for each of the nine phases in

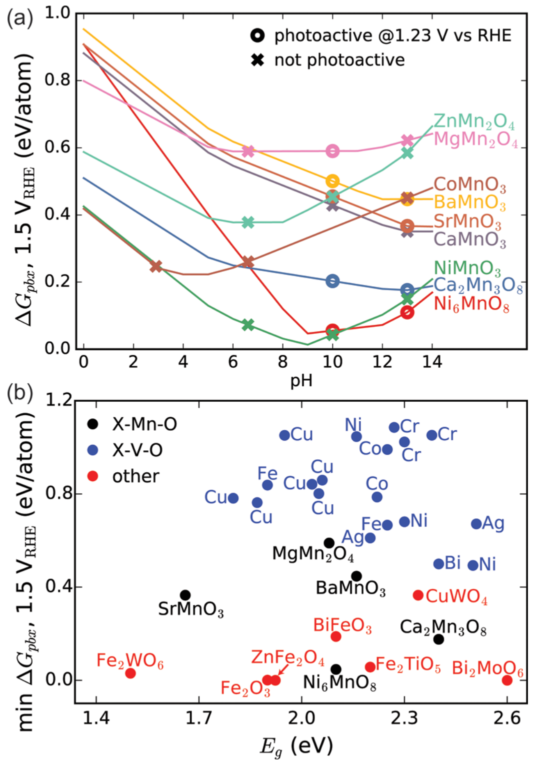

Figure 2. (a) Calculated above-Pourbaix-hull energies (ΔG_{pbx}) of nine identified phases from tier 6 at 1.5 V vs RHE as a function of electrolyte pH, with markers indicating the PEC photoactivity screening results. (b) Calculated minimum ΔG_{pbx} (pH 0−14) of 5 phases in tier 7, along with 26 phases previously identified as OER photoanodes with experimental band gap energy below 2.8 eV. The formula unit, band gap, and ΔG_{pbx} for each phase are listed in the SI (Table S2).

tier 6 of the pipeline. As illustrated in Figure S1, photoactivity for each phase was determined through inspection of composition-dependent measurements to ensure that the observed photoactivity was not due to the presence of a minority photoactive phase, a level of experimental validation enabled through the use of combinatorial materials science techniques. Tier 7 of the pipeline contains the five phases that exhibited photoactivity at the OER Nernstian potential (1.23 V vs RHE), which constitutes the discovery of OER photoactivity for these X−Mn−O materials. X-ray diffraction patterns for the five phases are provided in the SI (Figure S2) along with composition and thickness characterization by X-ray fluorescence.

To compare these five newly identified photoanodes with those of previous reports, Figure 2b shows the measured band gap energy and calculated minimum ΔG_{pbx} (pH 0−14) for all reported metal oxide OER photoanodes in the Materials Project with measured band gap energy below 2.8 eV. The interesting observations from this survey of metal oxide photoanodes include the following: (i) photoanodes that are not metal vanadates typically have a minimum $\Delta G_{pbx} < 0.8$ eV atom^{-1}, which may be generally understood by considering that highly unstable materials may corrode in experiments before photoactivity can be assessed; and (ii) the metal vanadates comprise the largest class of photoanodes despite their instability, which is likely due to self-passivation for many of these materials, combined with a propensity to remain photoactive after a passivation layer forms.[4] The previously reported, near-stable ($\Delta G_{pbx} < 0.5$ eV atom^{-1}) metal oxide photoanodes all contain Bi, W, and/or Fe, making the discovery of five X−Mn−O photoanodes an important expansion of the known OER photoanodes.

To further characterize these photoanodes and explore correlations among the electronic structure and Pourbaix stability, DFT calculation of the absolute valence band potential was performed for 29 phases that have minimum ΔG_{pbx} below 1.5 eV atom^{-1} (see Table S4). For these DFT calculations, we used the lowest-energy vacuum-terminated surface, as previously described.[14] Figure 3 includes three calculated properties of relevance for solar fuel photoanodes: band gap energy (E_g), band alignment to the OER equilibrium energy (E_{VBM}), and thermodynamic stability under operating conditions. Our calculated E_{VBM} values neglect effects of any surface dipole produced by the electrochemical double layer[9] or other details of the oxide−liquid interface. Therefore, they are best suited for studying trends among this family of phases and for identifying phases whose valence band lies at substantially higher energy than the undesirably deep values (approximately −8 eV) of oxides such as TiO_2 and WO_3. As a family of materials, these Mn-based oxides offer a wide range of E_{VBM} values, with four discovered photoanodes lying in the desirable −6.3 to −7.3 eV range. Comparing the properties of the photoactive and nonphotoactive phases in Figure 3 provides no clear distinction between these sets of materials, bringing into focus the importance of the native OER catalytic activity of the semiconductors in satisfying the tier 7 requirement, a line of inquiry that will be pursued in future research. For the present purposes, we note the presence of some correlation between E_{VBM} and ΔG_{pbx} at 1.5 V vs RHE, indicating that metal oxides with higher valence band energy are less stable under OER operating conditions. This further elucidates the historic difficulty in developing stable, efficient solar fuel photoanodes, as previously discussed with respect to the oxidative stability of photoaonode materials.[22]

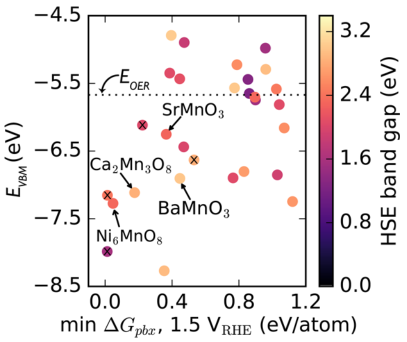

Figure 3. Calculated vacuum energy of the valence band maximum (E_{VBM}), HSE band gap energy (E_g), and minimum above-hull energy (ΔG_{pbx}) from pH 0 to 14 at 1.5 V vs RHE for 29 of the phases in tier 3 of the screening pipeline. The photoanodes discovered in the present work are denoted by phase labels ($MgMn_2O_4$ not shown), and four additional phases from tier 6 that were determined to not be photoactive are denoted by "x" markers.

Ni_6MnO_8 is a notable photoanode discovery due to its excellent stability in pH 9−12, and despite its reported catalytic activity[23] and measured 2.1 eV band gap, the OER external quantum efficiency (EQE) values from the high-throughput experiments are below 0.01% (see Table 1), guiding future investigations into improving the radiative efficiency and/or

DOI: 10.1021/acsenergylett.7b00607
ACS Energy Lett. 2017, 2, 2307−2312

Table 1. Nine Phases Identified in Tier 6 of the Screening Pipeline Listed with the Corresponding Band Gap Values from Both UV−Vis Experiments and HSE Calculations, Experimental EQE Values at 2 or 3 pH Values Per Phase, And the Calculated Minimum ΔG_{pbx} Value (pH 0−14)[a]

		band gap (eV)		EQE × 10^3 at 1.23 V_{RHE}, 385 nm				min ΔG_{pbx}, 1.5 V_{RHE}	
mp-id	phase	UV−vis	HSE	pH 2.9	pH 6.6	pH 10	pH 13	eV $atom^{-1}$	at pH
mp-19201	$CaMnO_3$	1.41	1.19			0	0	0.35	13
mp-19331	$NiMnO_3$	1.57	2.40		0	0	0	0.01	9
mp-568977	$SrMnO_3$	1.66	2.29			0.47	3.9	0.37	14
mp-18751	$ZnMn_2O_4$	1.88	2.13		0	0	0	0.38	6
mp-32006	$MgMn_2O_4$	2.08	2.39		0	1.0	0	0.59	6
mp-19442	Ni_6MnO_8	2.10	2.32			0.03	0.02	0.05	9
mp-19156	$BaMnO_3$	2.16	2.99			1.8	2.7	0.45	12
mp-24844	$CoMnO_3$	2.37	2.03	0	0		0	0.22	4
mp-18893	$Ca_2Mn_3O_8$	2.40	2.83			4.8	2.7	0.18	13

[a] The UV−vis band gaps are from indirect-allowed Tauc analysis (see Figure S2) with the exception of $CoMnO_3$ for which the direct-allowed band gap is listed and a lower-energy indirect gap may exist.

charge transport properties of this material. To provide context for the uniqueness of the other four discovered photoanodes, we return to the photoanodes survey of Figure 2b and note that, with the exception of the binary oxide Fe_2O_3, the previously reported photoanodes are ternary oxides that contain either two transition metals or a combination of Bi with a transition metal. Our discovery of (Mg, Ca, Sr, Ba)−Mn−O photoanodes broadens the space of OER photoelectrocatalyst materials to include combinations of alkaline earth and transition metal cations. The Mg-, Ca-, and Ba-containing phases have been studied as OER catalysts but not reported as photo(electro)catalysts for any reaction.[24−26] MnO_2 has shown some photoactivity for degradation of organics[27] and for oxygen evolution in the presence of amine ionic liquids.[28] The related Na-Birnessite structure was found to exhibit photoactivity only at high applied bias due to a very deep valence band near −8 eV vs vacuum.[29] A notable similarity in the tier 7 phases is the combination of Mn^{4+} with a +2 cation (Ni, Sr, Mg, Ba, or Ca), creating a family of structures with substantially improved photoelectrochemical properties compared to the reported Mn^{4+} materials noted above.

With respect to the Pourbaix stability, $Ca_2Mn_3O_8$, $SrMnO_3$, and $BaMnO_3$ are unique among the X−Mn−O phases due to their decreasing ΔG_{pbx} with increasing pH (see Figure 2a), prompting further PEC characterization in the pH 13 electrolyte (Figure 4). In the cyclic voltammetry (CV) measurements of Figure 4a, the lowest potential at which anodic photocurrent is observed is near 1 V vs RHE for $SrMnO_3$, below 0.9 V vs RHE for $Ca_2Mn_3O_8$, and below 0.8 V vs RHE for $BaMnO_3$, where estimation of the illuminated open-circuit potential of the latter two phases is obscured by the onset of cathodic dark current. From inspection of the Pourbaix diagrams for these phases, this dark current is likely due to the electrochemical reduction of Mn^{4+} to Mn^{3+}. The persistence of this electrochemical reduction under illumination suggests a spatially variable surface potential wherein some sites proceed with photodriven OER (at a photoinduced potential where Mn remains in the +4 state) while others experience the electrochemical potential of the electrochemical back contact (where Mn is reduced to the +3 state). The measured signal is thus a combination of a cathodic electrochemical and an anodic photoelectrochemical process. These observations motivate future studies wherein the optimal surfaces are identified and synthesized to reveal the true flat band potential and photovoltage of these semiconductors, which may be substantially better than these initial experiments suggest. In addition, it is worth noting that all three phases exhibit dark OER electrocatalytic activity[24−26] within a respectable 0.4 V overpotential window and that photocurrent exhibited by each

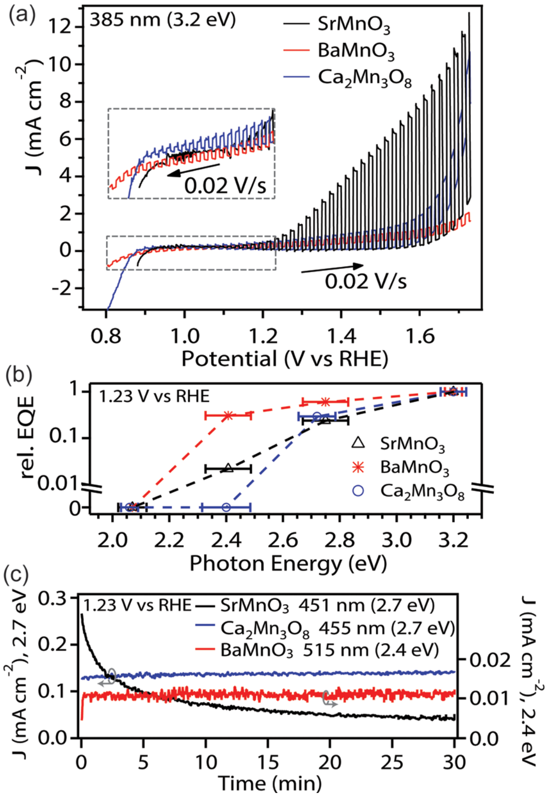

Figure 4. (a) Front-side toggled-illumination (385 nm LED, 0.5 s on and 0.5 s off) cyclic voltammograms of $SrMnO_3$, $BaMnO_3$, and $Ca_2Mn_3O_8$ starting with a cathodic sweep from 1.23 V vs RHE (inset) and finishing with an anodic sweep to 1.73 V vs RHE in pH 13 electrolyte. (b) Spectral EQE at 1.23 V vs RHE in the same electrolyte, normalized by the EQE value at 3.2 eV illumination. The horizontal error bars correspond to the width of the respective LED emission spectrum (see Table S3). (c) PEC stability in pH 13 electrolyte as characterized by 30 min chopped-illumination photocurrent measurements at 1.23 V vs RHE under 451, 515, and 455 nm illumination for $SrMnO_3$, $BaMnO_3$, and $Ca_2Mn_3O_8$, respectively. The right vertical axis in (c) corresponds to the data for $BaMnO_3$ (red).

phase increases substantially between 1.23 and 1.6 V vs RHE. The $SrMnO_3$ photocurrent approaches 9 mA cm^{-2}, which for this illumination configuration (385 nm LED) corresponds to an EQE of approximately 15%, giving hope that substantial improvements to the measured EQE of each of these phases (Table 1) can be obtained through materials optimization.

While all three phases exhibit desirable band gap energies at or below 2.4 eV, recent work has demonstrated that the onset of photoactivity may be substantially higher than the band gap energy in complex metal oxides.[30] To explore the relationship of the measured band gap energy and lowest photon energy at which photocurrent is observed, the EQE for each phase was measured at 1.23 V vs RHE at four photon energies, as shown in Figure 4b. To observe the decrease in EQE with decreasing photon energy, the values for each phase are scaled by the value at the highest photon energy. While $SrMnO_3$ exhibits the lowest band gap energy of 1.66 eV, its onset of OER activity is in excess of 2.4 eV, motivating investigation into possible causes for the inactivity of low-energy absorption in this material. Both $BaMnO_3$ and $Ca_2Mn_3O_8$ exhibit photocurrent onset commensurate with the respective band gap energy.

To characterize the initial stability of each phase, 30 min chopped illumination experiments were performed at 1.23 V vs RHE using a LED above the photon energy of photocurrent onset. It is worth noting that these experiments were performed with rapid solution flow to keep the anolyte's ionic concentrations low, creating an aggressive screen for operational stability. $SrMnO_3$ is the only phase that exhibits degradation, with the photocurrent of $Ca_2Mn_3O_8$ drifting up by approximately 10% over the initial 10 min and then remaining constant and the photocurrent of $BaMnO_3$ remaining relatively constant through the experiment. With its 2.16 eV band gap energy, OER photoactivity over a substantial fraction of the visible spectrum, the opportunity for attaining a sizable photovoltage, and excellent PEC stability, $BaMnO_3$ emerges as perhaps the most promising photoanode from this suite of experiments. As shown in Figure S2, it is a direct or pseudodirect semiconductor with a band gap energy of approximately 2.2 eV. Previous work on photoluminescent $BaMnO_3$ nanorods indicates that the radiative efficiency of this phase may be improved with optimized synthesis,[31] highlighting that additional study of all five discovered photoanodes is required to establish their performance limitations for solar fuel generation and beyond.

■ ASSOCIATED CONTENT

Supporting Information

The Supporting Information is available free of charge on the ACS Publications website at DOI: 10.1021/acsenergylett.7b00607.

> Experimental details for physical vapor deposition (Table S1); calculated above-Pourbaix-hull energies (ΔG_{pbx}) for 31 phases (Table S2); illumination sources for photoelectrochemistry (Table S3); composition-photoactivity-phase maps (Figure S1); XRD for tier 7 phases (Figure S2); Tauc plots for tier 6 phases (Figure S3); and full screening results for the 51 phases in tier 2 (Table S4) (PDF)

■ AUTHOR INFORMATION

Corresponding Authors

*E-mail: kristinpersson@berkeley.edu (K.A.P.).
*E-mail: jbneaton@berkeley.edu (J.B.N.).
*E-mail: gregoire@caltech.edu (J.M.G.).

ORCID

Santosh K. Suram: 0000-0001-8170-2685
John M. Gregoire: 0000-0002-2863-5265

Author Contributions

◆A. Shinde, S. K. Suram, and Q. Yan contributed equally.

Notes

The authors declare no competing financial interest.

■ ACKNOWLEDGMENTS

This material is based upon work performed by the Joint Center for Artificial Photosynthesis, a DOE Energy Innovation Hub, supported through the Office of Science of the U.S. Department of Energy under Award Number DE-SC0004993. Computational work was additionally supported by the Materials Project (Grant No. EDCBEE) through the U.S. Department of Energy (DOE), Office of Basic Energy Sciences, Materials Sciences and Engineering Division, under Contract DE-AC02-05CH11231. Work at the Molecular Foundry was supported by the Office of Science, Office of Basic Energy Sciences, of the U.S. DOE under Contract DE-AC02-05CH11231. Computational resources were also provided by the DOE through the National Energy Supercomputing Center, a DOE Office of Science User Facility supported by the Office of Science of the U.S. DOE under Contract DE-AC02-05CH11231. Use of the Stanford Synchrotron Radiation Lightsource, SLAC National Accelerator Laboratory, was supported by the U.S. Department of Energy, Office of Science, Office of Basic Energy Sciences under Contract No. DE-AC02-76SF00515.

■ REFERENCES

(1) Dionysiou, D. D.; Li Puma, G.; Ye, J.; Schneider, J.; Bahnemann, D. *Photocatalysis*; The Royal Society of Chemistry, 2016.

(2) Ferreira, K. N.; Iverson, T. M.; Maghlaoui, K.; Barber, J.; Iwata, S. Architecture of the Photosynthetic Oxygen-Evolving Center. *Science* **2004**, *303*, 1831−1838.

(3) Najafpour, M. M.; Renger, G.; Holynska, M.; Moghaddam, A. N.; Aro, E. M.; Carpentier, R.; Nishihara, H.; Eaton-Rye, J. J.; Shen, J. R.; Allakhverdiev, S. I. Manganese Compounds as Water-Oxidizing Catalysts: From the Natural Water-Oxidizing Complex to Nanosized Manganese Oxide Structures. *Chem. Rev.* **2016**, *116*, 2886−2936.

(4) Zhou, L.; Yan, Q.; Yu, J.; Jones, R. J. R.; Becerra-Stasiewicz, N.; Suram, S. K.; Shinde, A.; Guevarra, D.; Neaton, J. B.; Persson, K. A.; Gregoire, J. M. Stability and Self-Passivation of Copper Vanadate Photoanodes under Chemical, Electrochemical, and Photoelectrochemical Operation. *Phys. Chem. Chem. Phys.* **2016**, *18*, 9349−9352.

(5) Hu, S.; Shaner, M. R.; Beardslee, J. A.; Lichterman, M.; Brunschwig, B. S.; Lewis, N. S. Amorphous Tio2 Coatings Stabilize Si, Gaas, and Gap Photoanodes for Efficient Water Oxidation. *Science* **2014**, *344*, 1005−1009.

(6) Lichterman, M. F.; Sun, K.; Hu, S.; Zhou, X.; McDowell, M. T.; Shaner, M. R.; Richter, M. H.; Crumlin, E. J.; Carim, A. I.; Saadi, F. H.; Brunschwig, B. S.; Lewis, N. S. Protection of Inorganic Semiconductors for Sustained, Efficient Photoelectrochemical Water Oxidation. *Catal. Today* **2016**, *262*, 11−23.

(7) Guevarra, D.; Shinde, A.; Suram, S. K.; Sharp, I. D.; Toma, F. M.; Haber, J. A.; Gregoire, J. M. Development of Solar Fuels Photoanodes through Combinatorial Integration of Ni-La-Co-Ce Oxide Catalysts on Bivo4. *Energy Environ. Sci.* **2016**, *9*, 565−580.

(8) Zachaus, C.; Abdi, F. F.; Peter, L. M.; van de Krol, R. Photocurrent of Bivo4 Is Limited by Surface Recombination, Not Surface Catalysis. *Chem. Sci.* **2017**, *8*, 3712−3719.

(9) Stevanovic, V.; Lany, S.; Ginley, D. S.; Tumas, W.; Zunger, A. Assessing Capability of Semiconductors to Split Water Using Ionization Potentials and Electron Affinities Only. *Phys. Chem. Chem. Phys.* **2014**, *16*, 3706−3714.

(10) Hardee, K. L.; Bard, A. J. Semiconductor Electrodes: V. The Application of Chemically Vapor Deposited Iron Oxide Films to Photosensitized Electrolysis. *J. Electrochem. Soc.* **1976**, *123*, 1024−1026.

(11) Valenzuela, M. A.; Bosch, P.; Jiménez-Becerrill, J.; Quiroz, O.; Páez, A. I. Preparation, Characterization and Photocatalytic Activity of Zno, Fe2o3 and Znfe2o4. *J. Photochem. Photobiol., A* **2002**, *148*, 177−182.

(12) De Haart, L. G. J.; Blasse, G. Photoelectrochemical Properties of Ferrites with the Spinel Structure. *Solid State Ionics* **1985**, *16*, 137−139.

(13) Tang, D.; Mabayoje, O.; Lai, Y.; Liu, Y.; Mullins, C. B. Enhanced Photoelectrochemical Performance of Porous Bi2moo6 Photoanode by an Electrochemical Treatment. *J. Electrochem. Soc.* **2017**, *164*, H299−H306.

(14) Yan, Q.; Yu, J.; Suram, S. K.; Zhou, L.; Shinde, A.; Newhouse, P. F.; Chen, W.; Li, G.; Persson, K. A.; Gregoire, J. M.; Neaton, J. B. Solar Fuels Photoanode Materials Discovery by Integrating High-Throughput Theory and Experiment. *Proc. Natl. Acad. Sci. U. S. A.* **2017**, *114*, 3040−3043.

(15) Zhou, L.; Yan, Q.; Shinde, A.; Guevarra, D.; Newhouse, P. F.; Becerra-Stasiewicz, N.; Chatman, S. M.; Haber, J. A.; Neaton, J. B.; Gregoire, J. M. High Throughput Discovery of Solar Fuels Photoanodes in the CuO−V2O5 System. *Adv. Energy Mater.* **2015**, *5*, 1500968.

(16) Seabold, J. A.; Neale, N. R. All First Row Transition Metal Oxide Photoanode for Water Splitting Based on Cu3v2o8. *Chem. Mater.* **2015**, *27*, 1005−1013.

(17) Jain, A.; Ong, S. P.; Hautier, G.; Chen, W.; Richards, W. D.; Dacek, S.; Cholia, S.; Gunter, D.; Skinner, D.; Ceder, G.; Persson, K. A. Commentary: The Materials Project: A Materials Genome Approach to Accelerating Materials Innovation. *APL Mater.* **2013**, *1*, 011002.

(18) Perdew, J. P.; Burke, K.; Ernzerhof, M. Generalized Gradient Approximation Made Simple. *Phys. Rev. Lett.* **1996**, *77*, 3865−3868.

(19) Heyd, J.; Scuseria, G. E.; Ernzerhof, M. Hybrid Functionals Based on a Screened Coulomb Potential. *J. Chem. Phys.* **2006**, *124*, 219906.

(20) Heyd, J.; Peralta, J. E.; Scuseria, G. E.; Martin, R. L. Energy Band Gaps and Lattice Parameters Evaluated with the Heyd-Scuseria-Ernzerhof Screened Hybrid Functional. *J. Chem. Phys.* **2005**, *123*, 174101.

(21) Tahir, M.; Pan, L.; Idrees, F.; Zhang, X.; Wang, L.; Zou, J.-J.; Wang, Z. L. Electrocatalytic Oxygen Evolution Reaction for Energy Conversion and Storage: A Comprehensive Review. *Nano Energy* **2017**, *37*, 136−157.

(22) Chen, S.; Wang, L.-W. Thermodynamic Oxidation and Reduction Potentials of Photocatalytic Semiconductors in Aqueous Solution. *Chem. Mater.* **2012**, *24*, 3659−3666.

(23) Menezes, P. W.; Indra, A.; Levy, O.; Kailasam, K.; Gutkin, V.; Pfrommer, J.; Driess, M. Using Nickel Manganese Oxide Catalysts for Efficient Water Oxidation. *Chem. Commun.* **2015**, *51*, 5005−5008.

(24) Ramírez, A.; Bogdanoff, P.; Friedrich, D.; Fiechter, S. Synthesis of $Ca_2mn_3o_8$ Films and Their Electrochemical Studies for the Oxygen Evolution Reaction (Oer) of Water. *Nano Energy* **2012**, *1*, 282−289.

(25) Maitra, U.; Naidu, B. S.; Govindaraj, A.; Rao, C. N. R. Importance of Trivalency and the Eg1 Configuration in the Photocatalytic Oxidation of Water by Mn and Co Oxides. *Proc. Natl. Acad. Sci. U. S. A.* **2013**, *110*, 11704−11707.

(26) Xu, Y.; Tsou, A.; Fu, Y.; Wang, J.; Tian, J.-H.; Yang, R. Carbon-Coated Perovskite Bamno3 Porous Nanorods with Enhanced Electrocatalytic Perporites for Oxygen Reduction and Oxygen Evolution. *Electrochim. Acta* **2015**, *174*, 551−556.

(27) Chan, Y. L.; Pung, S. Y.; Hussain, N. S.; Sreekantan, S.; Yeoh, F. Y. Photocatalytic Degradation of Rhodamine B Using MnO_2 and ZnO Nanoparticles. In *Isesco Conference on Nanomaterials and Applications 2012*; Umar, A. A., Salleh, M. M., Yahaya, M., Eds.; Trans Tech Publications Ltd: Stafa-Zurich, Switzerland, 2013; Vol. *756*, pp 167−174.

(28) Zhou, F.; McDonnell-Worth, C.; Li, H.; Li, J.; Spiccia, L.; Macfarlane, D. R. Enhanced Photo-Electrochemical Water Oxidation on Mnox in Buffered Organic/Inorganic Electrolytes. *J. Mater. Chem. A* **2015**, *3*, 16642−16652.

(29) Pinaud, B. A.; Chen, Z.; Abram, D. N.; Jaramillo, T. F. Thin Films of Sodium Birnessite-Type Mno_2: Optical Properties, Electronic Band Structure, and Solar Photoelectrochemistry. *J. Phys. Chem. C* **2011**, *115*, 11830−11838.

(30) Jiang, C.-M.; Farmand, M.; Wu, C. H.; Liu, Y.-S.; Guo, J.; Drisdell, W. S.; Cooper, J. K.; Sharp, I. D. Electronic Structure, Optoelectronic Properties, and Photoelectrochemical Characteristics of Γ-$Cu_3v_2o_8$ Thin Films. *Chem. Mater.* **2017**, *29*, 3334−3345.

(31) Balamurugan, S.; Mini, K. S. A.; Raja, T. S. G.; Parthiban, P. Mechano-Thermal Synthesis and Characterization of Bamno3 Nano-Needles. *J. Nanosci. Nanotechnol.* **2015**, *15*, 5978−5986.